APPLIED SCIENCES AND ENGINEERING

Adaptive metalenses with simultaneous electrical control of focal length, astigmatism, and shift

Alan She, Shuyan Zhang, Samuel Shian, David R. Clarke,* Federico Capasso*

Focal adjustment and zooming are universal features of cameras and advanced optical systems. Such tuning is usually performed longitudinally along the optical axis by mechanical or electrical control of focal length. However, the recent advent of ultrathin planar lenses based on metasurfaces (metalenses), which opens the door to future drastic miniaturization of mobile devices such as cell phones and wearable displays, mandates fundamentally different forms of tuning based on lateral motion rather than longitudinal motion. Theory shows that the strain field of a metalens substrate can be directly mapped into the outgoing optical wavefront to achieve large diffraction-limited focal length tuning and control of aberrations. We demonstrate electrically tunable large-area metalenses controlled by artificial muscles capable of simultaneously performing focal length tuning (>100%) as well as on-the-fly astigmatism and image shift corrections, which until now were only possible in electron optics. The device thickness is only 30 μm. Our results demonstrate the possibility of future optical microscopes that fully operate electronically, as well as compact optical systems that use the principles of adaptive optics to correct many orders of aberrations simultaneously.

INTRODUCTION

There has been a wide variety of work on tunable optical devices, particularly tunable focus lenses (that is, varifocal lenses), with important applications in imaging and adaptive vision. Focus tuning is usually performed by the mechanical movement of rigid elements (*1*), which provides great imaging performance at the expense of bulk and inertially limited speed. Other applications include liquid crystal–based spatial light modulators (*2*–*4*), which can be relatively high speed and capable of correcting for aberrations but are limited in resolution and polarization dependence; fluid-based tunable lenses (*5*–*10*) (including those incorporating elastomeric materials), which can be high speed, have a wide tuning range, and are relevant for small-scale devices but whose exact surface curvature is difficult to control (for example, coma is observed when the lens is placed vertically, as a result of gravity); tunable acoustic gradient index lenses (*11*), which can be tuned at high speeds but must be used stroboscopically; and electro-optic lenses (*12*), which are high speed but polarization-sensitive. In astronomy (*13*, *14*) and microscopy (*15*), adaptive optics uses deformable mirrors to correct for wavefront distortions but must operate in reflection.

Recently, flat lens technology based on metasurfaces (*16*), which control the wavefront of light using subwavelength-spaced nanostructures, has shown considerable potential in optical performance while reducing element thickness to the micrometer level, opening up new opportunities to replace bulk optical devices with thin, flat, lightweight devices (*17*, *18*). Instead of moving several optical components longitudinally along the optical axis as in telephoto lenses and autofocus cameras, in metasurfaces, lateral control can be used to vary focus and magnification, as well as other adaptive optics capabilities (*13*–*15*), and to leverage their flatness. Reported recently were mechanically tunable metasurfaces in which metasurfaces were embedded in stretchable substrates (*19*–*21*) but were limited in size (less than a millimeter in diameter), required external apparatuses to apply strain, and had inherent speed limitations, restricting their applications. In addition, no theoretical analysis of the effect of strain field tuning on optical aberrations was presented. Here, the combination of metasurface optics and dielectric elastomer actuators (DEAs)—sometimes referred to as artificial muscles (*22*) in soft robotics—offers a versatile platform for electrically tunable optical devices through the design of phase, amplitude, and polarization profiles.

A flat lens can be constructed by a metasurface with the following hyperboloidal phase profile (*17*)

$$\phi(r) = \pm k\left(\sqrt{r^2 + f^2} - f\right) \quad (1)$$

where k is the wave number, r is the radial position, f is the focal length, and the positive or negative sign is applied for diverging or converging lenses, respectively (Fig. 1A). A lens described by Eq. 1 focuses light that is free of spherical aberrations for normal incidence (infinity-corrected) illumination. By combining this metasurface with a DEA, the lens can be made electrically tunable.

A DEA (*22*), which is a type of electroactive polymer, is effectively a compliant parallel plate capacitor that stretches when a voltage or electrical field is applied (*23*). By using a soft elastomer (for example, polyacrylate and silicone rubber) as a dielectric, together with transparent, stretchable electrodes (*5*), the configuration is slightly compressed in the thickness direction when a voltage is applied. As elastomers conserve volume on deformation, thinning results in a lateral expansion that can be very large (~500%) (*24*). The attainable actuation strain is a function of the electrostatically induced Maxwell stress, the constitutive deformation behavior of the elastomers, and the mechanical configuration of the elastomers and electrodes (*25*). Bonding a metasurface with the DEA couples the metasurface profile to voltage-induced stretching, which is approximately uniform over a single electrode area. Effectively, the coordinates of the metasurface scale by a stretch factor, s ($s = 1 + \varepsilon_L$, where ε_L is lateral strain), such that $r \rightarrow r/s$

$$\phi_{\text{stretched}}(r, s) = \pm k\left(\sqrt{(r/s)^2 + f_0^2} - f_0\right) \quad (2)$$

where f_0 is the focal length without actuation (Fig. 1B). The focal length of Eq. 2 varies quadratically with stretch: $f(s) = s^2 f_0$ (see

Harvard John A. Paulson School of Engineering and Applied Sciences, Cambridge, MA 02138, USA.
*Corresponding author. Email: clarke@seas.harvard.edu (D.R.C.); capasso@seas.harvard.edu (F.C.)

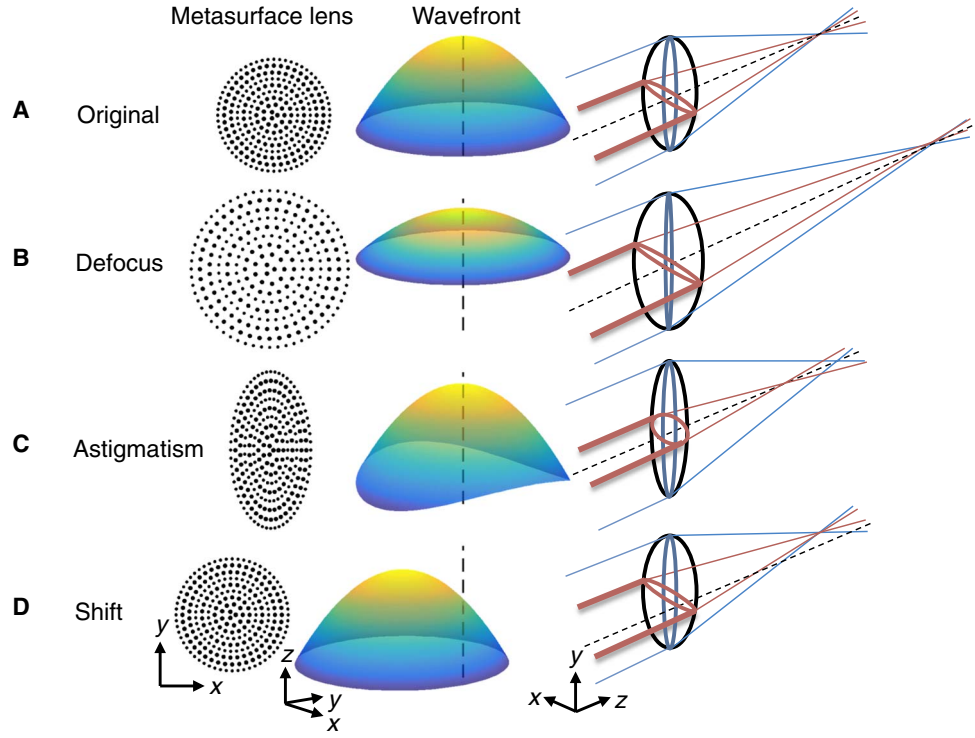

Fig. 1. Principle of strain field–mediated tunable metalens. A metasurface (left column) is constructed by digitizing an analog optical phase profile on a flat surface into discrete cells, each of which contains a metasurface element that locally imparts the required phase shift to the incident light to reconstruct the desired wavefront (middle column; dashed line: optical axis). The wavefront generated by the metasurface determines the subsequent beam shaping (right column). (**A**) Original: metasurface without stretch. (**B**) Defocus: metasurface with uniform and isotropic stretch. (**C**) Astigmatism: metasurface under asymmetric stretch. (**D**) Shift: metasurface displaced laterally in the *x*,*y* plane.

Materials and Methods). The voltage dependence of the focal length provided by the DEA is

$$\frac{f}{f_0} = \frac{1}{1 - (\varepsilon/Y)(V/t)^2} \tag{3}$$

where V is the voltage and ε, Y, and t are the permittivity, Young's modulus, and dielectric layer thickness, respectively. Tuning in this manner introduces negligible aberrations (fig. S1; see also Materials and Methods).

In practice, an infinite number of wavefront aberrations can exist and can be quantified in terms of Zernike polynomials (table S1). In most cases, the eight lowest terms are sufficient: piston, tip, tilt, defocus, oblique and vertical astigmatism, and vertical and horizontal coma. Because the Zernike terms are linear and orthogonal, specific aberrations can be targeted and tuned by introducing the appropriate displacement field to the phase profile. In general, applying the stress of a particular configuration induces a strain field, resulting in a displacement field. The displacement field can be regarded as the sum of deformation ($\bar{A}$) and rigid-body displacement ($\bar{B}$) components, in which the transformed coordinates can be expressed as follows: $\bar{x}' = \bar{A}(x, \eta) + \bar{B}(\eta)$, where η is a parameter (for example, voltage) and $\bar{x}$ and $\bar{x}'$ are the original and transformed coordinates, respectively (*26*). For metasurfaces, the phase profile transforms as $\phi(x, y) \rightarrow \phi(x', y')$. The rigid-body displacement is simply a lateral shift of the entire phase profile, whereas the deformation changes the shape or size, resulting in a shape change of the passing wavefront. In the case of asymmetric biaxial strain, the coordinates of the phase profile transform as $(x, y) \rightarrow (x/s_x, y/s_y)$: $\phi = \pm k\left(\sqrt{(x/s_x)^2 + (y/s_y)^2 + f_0^2} - f_0\right)$, where $s_x \neq s_y$. Light propagating along two perpendicular planes experiences different focal lengths, which is astigmatism. Thus, through an electrically controlled strain field, it is possible to create the optical analog of image shift and stigmators (Fig. 1, C and D) found in electron microscopes (*27*).

RESULTS

Adaptive metalens design

A polarization-insensitive, converging metalens [diameter (ø) = 6 mm, f = 50 mm, λ = 1550 nm; see Fig. 2A] was combined with a DEA constructed using transparent polyacrylate elastomers with transparent, stretchable patterned electrodes made of single-walled carbon nanotubes (SWCNTs) (figs. S2 and S3; see also Materials and Methods) (*28*). The DEA was measured to exhibit large transparency windows in the visible, near-infrared, and mid-infrared spectra (fig. S4). Focal length tuning was implemented by applying a voltage through the center electrode V_5 to increase focal length or from V_1 through V_4 to decrease focal length (Figs. 1B and 2), corresponding to lateral expansion or contraction of post spacings, respectively. Control of vertical astigmatism in the *x*,*y* directions ("*x*,*y* stigmators") was implemented by activating opposing pairs of electrodes (Figs. 1C and 2). Image shift was implemented by activating one peripheral electrode, V_1 through V_4, such that its expansion caused the entire metasurface to shift in space (Figs. 1D and 2). Any combination of actuations, each implemented using different voltages, was also possible (fig. S5).

Two types of devices were fabricated and measured: a single-layer (SL) device and a double-layer (DL) device (fig. S5A). Although the SL

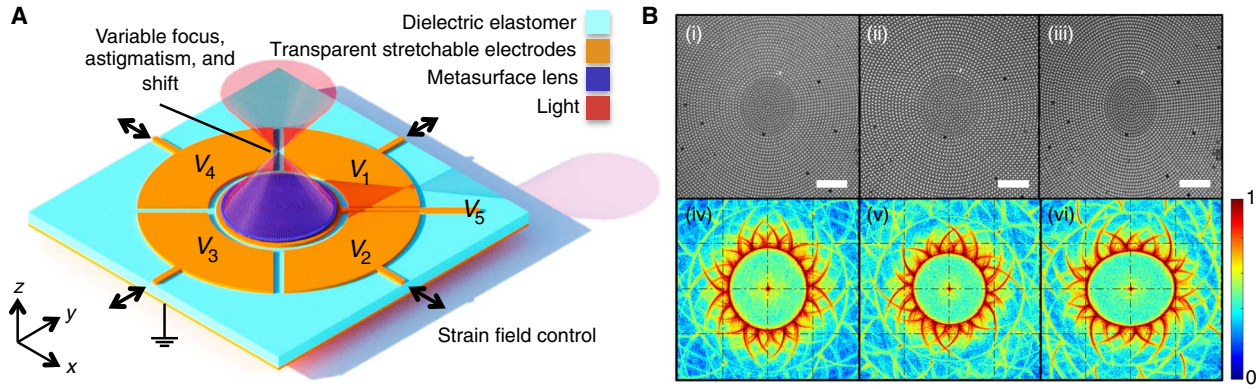

Fig. 2. DEA metalens device design. (**A**) A schematic of the device in which a metalens and a DEA with five addressable electrodes are combined to allow for electrical control over the strain field of the metasurface. (**B**) Optical microscope images (scale bars, 20 μm) at (i) no voltage, (ii) 2.5 kV applied to the center electrode (V_5), and (iii) 2.75 kV applied to tune *x* astigmatism (concurrently, V_1 and V_3). The dark spots are defects (either missing or tilted silicon posts) introduced during the transfer process. The corresponding two-dimensional Fourier transforms (FTs) of (i) to (iii) are shown in (iv) to (vi), respectively (normalized amplitudes).

device demonstrated better tunability compared to the DL device [for the same applied voltage, the SL device was stretched more than the DL device on account of the lesser stiffness introduced by the smaller intermediate elastomer layer (IEL)], most of the data presented were those of the DL device because of its higher quality. The maximum voltage used was 3 kV, producing $s = 1.41$ (SL) and $s = 1.15$ (DL) (Fig. 3).

Focus measurement

Focal length was measured by scanning a camera along the *z* axis for varying voltages (fig. S6). From $f_0 = 50$ mm, the DL focal length was tuned by 15 mm ($\Delta f/f_0 = 30\%$) with 3 kV (Fig. 3C) and closely followed the predicted voltage relation (Eq. 3 and fig. S7), whereas the SL device exhibited greater (107%) focal length modulation (Fig. 3C, inset). The focusing efficiency (DL), defined as the ratio of focused optical power to incident power (fig. S6C), showed a high average efficiency of 62.5% with little variation throughout the tuning range (Fig. 3B). The near-constant efficiency was due to the relatively small stretching range used, which allowed the posts to maintain subwavelength spacing, and to the high optical confinement factor (the calculated confinement factor, defined as $\Gamma = P_{inside\_post}/P_{total}$, is 0.71 ± 0.01 and 0.69 ± 0.01 for $s = 1$ and $s = 1.09$, respectively) within the posts as a result of the large index contrast (*29*), which minimized the effect of changes in gap size. At 0 and 1 kV, focal spot sizes ($1/e^2$ full beam waist) were measured and compared to the theoretical diffraction-limited spot sizes (ø = 6 mm, $M^2 = 1.3$): 34.4 ± 1.1 μm (diffraction limit, 21.4 μm) and 37.7 ± 2.8 μm (diffraction limit, 22.7 μm), respectively (Fig. 3A). Possible explanations for these differences included fabrication errors and small distortions introduced when the elastomer was initially pressed onto the metasurface. Because of setup constraints, images of the focal spots at higher voltages (>1 kV) were obtained directly by the camera without magnification (Fig. 3B).

Stigmator and shifter measurement

The effect of the *x* stigmator, which squeezed the phase profile into an elliptical shape, was measured to show asymmetric yet spatially uniform biaxial strain according to FT images (Fig. 2B), indicating good stigmator performance corroborated by the Zernike transform (Fig. 3D). The sharpness of the FTs is indicative of the quality of the lens, whereas the radii of the first-order annulus, corresponding to the reciprocal space representation of the radial periodicity between posts, are a measure of the biaxial stretch. The features seen in the FTs are signatures of symmetries used by the metasurface design algorithm.

The *x*,*y* shifters were able to shift the image in all cardinal directions by applying appropriate control voltages (Fig. 3E). The observed control asymmetry was likely due to residual asymmetric stiffness around the periphery of the device because three different structures needed to be concentrically aligned during fabrication: the outer frame, the electrodes, and the metasurface. Shift-induced distortions of the metasurface were minimal (fig. S8).

Reliability test

The reliability of the device was tested with a sinusoidal voltage from 2 to 100 Hz at an amplitude of 2.5 kV (movie S1). The device did not fail, nor was image quality observed to degrade after >1000 cycles. The mechanical robustness of the device was attributed to the relatively small actuation strains applied. By applying a voltage square wave, the response time was measured to be 33 ± 3 ms (fig. S9) and was mainly limited by the elastomer viscoelasticity, charge transfer, and dissipation time in SWCNT electrodes. Dielectric breakdown was measured at ~3.5 kV, when the current began to flow through the dielectric, damaging the device. The electrical breakdown was a "soft" breakdown associated with local burning through the elastomer, and the same devices were able to resume operation after cycling power. This self-healing feature was attributed to the burning and subsequent clearing of SWCNT electrodes around the breakdown location, which prevented further electrical shorting.

DISCUSSION

We have demonstrated an electrically tunable metalens with multiple, simultaneous control parameters, as well as a centimeter-scale metalens. In comparison to existing systems, our device offers a route to extremely compact, lightweight transmissive adaptive optics with large, well-controlled tunability and high-definition (subwavelength) phase profiles. It is capable of performing focus tuning and aberration control simultaneously. In its current form, it is limited in speed and requires a high operating voltage. We note that our demonstration of astigmatism and image shift tuning is important for the correction of misalignment in optical systems based on metasurfaces. By using thinner elastomers (*30*) (operating voltage <12 V) or miniature high-voltage components

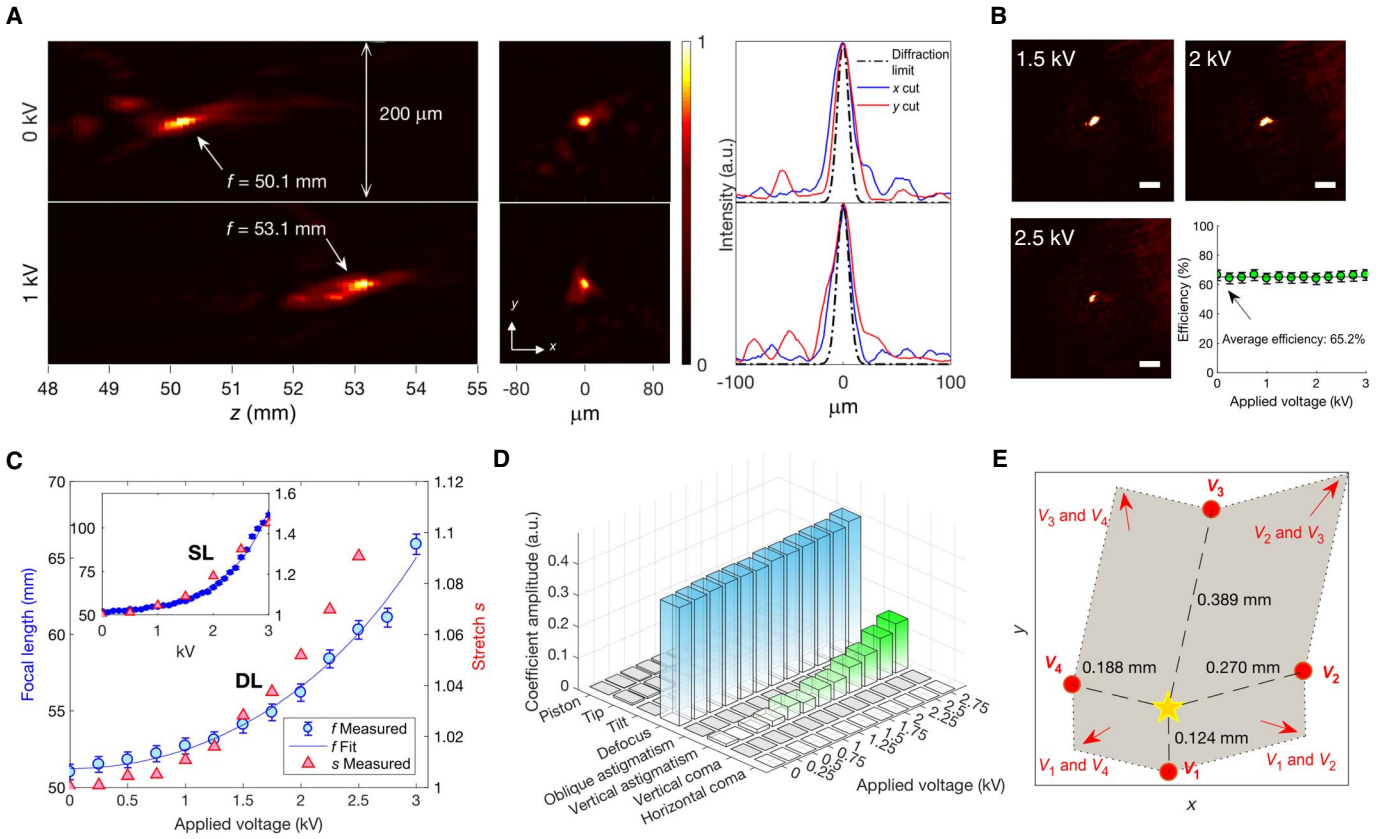

Fig. 3. Measurement of tuning. (**A**) (Left) *Z*-scan of the intensity profile showing two distinct focal lengths. (Center) Image of focal spot intensity profile (that is, *x*-*y* cross sections at the position of maximum intensity). (Right) Line scans of focal spot intensity image in the *x* (blue) and *y* (red) directions in comparison to the theoretical diffraction-limited spot size (black). a.u., arbitrary units. (**B**) Additional images of the focal spots at 1.5, 2, and 2.5 kV are shown, captured directly by the camera without the microscope objective (scale bars, 200 μm). (Bottom right) Measured focusing efficiency for varying voltages (see fig. S6C for setup). (**C**) Measurement of focal length tuning using the center electrode V_5 for DL and SL (inset) devices. Blue circles represent optical measurement of device focal length as a function of applied voltage. The solid blue line indicates the fit of focal length data to Eq. 3 ($R^2 = 0.9915$). Red triangles represent measurement of stretch as a function of the applied voltage. (**D**) Measured Zernike coefficients of the phase profile (calculated from microscope images of the lens center) showing targeted tuning of vertical astigmatism, whereas other Zernike coefficients exhibit little change. The large defocus value represents the designed focal power of the lens. (**E**) Measurement of *x*,*y* shift control showing two-axis displacement control from the focus position at 0 kV (yellow star) to various positions (red dots) as 1.9 kV is applied. The gray shaded area shows possible displacements, which can be accessed by concurrently activating combinations of electrodes.

that are commonly found in devices such as mobile phones (for example, flash modules), voltage requirements may be substantially reduced. Speed may be further increased to the microsecond time scale (*31*). Custom-made elastomers such as silicone-based elastomers (*30*) could provide a direct path for these improvements because elastomer dimensions and electromechanical properties could be tailored during processing. However, in addition to the mechanical stability of devices, the use of thinner or different elastomers requires adaptation and optimization of other aspects, such as the choice of stretchable electrodes and the lens transfer process. Devices can be made using the same method, with diameters ranging from micrometers to centimeters. These desirable characteristics are suitable for integration in size- and weight-limited imaging systems and wearable devices. Our results demonstrate the feasibility of embedded autofocus, optical zoom, image stabilization, and adaptive optics, which are expected to become essential for future chip-scale image sensors and head-mounted optics such as everyday eyeglasses and virtual reality hardware. Furthermore, the device's flat construction and inherently lateral actuation without the need for motorized parts allow for highly stackable systems such as those found in stretchable electronic eye camera sensors (*32*), providing possibilities for new kinds of imaging systems.

MATERIALS AND METHODS

Experimental design

Metalens design

The unit cell of the design is shown in fig. S3A. The height (*h*) of the posts was 950 nm. By varying the diameter of the posts ($d = 810$ to 990 nm), a phase coverage of close to 2π and a high uniform transmission amplitude response were achieved (fig. S3B). These data were used as a lookup table to digitize the phase profile. Post diameters with low transmission values (for example, $d = 860$ and 870 nm) were excluded from the lookup table. Given the circular shape of the post structures, the phase and amplitude responses were independent of the polarization of the incoming light. The phase profile was realized using subwavelength antennas with fixed edge-to-edge separation (fig. S3C), by which the placement of antennas was made denser than that with conventional fixed center-to-center separation. Hence, the size of the unit cell (*u*) was equal to the sum of the

post diameter (d) and the constant edge-to-edge spacing (e): $u = d + e$. In our design, we chose the edge-to-edge spacing to be 650 nm, which was determined by the feature size of the stepper used and the length scale to avoid interaction between neighboring antennas.

Selection of materials

A wide range of elastomers with varying chemical, mechanical, and dielectric properties have been reported for electrostatic actuation (*22*). We chose an off-the-shelf acrylate elastomer [VHB Tape 4905 (hereafter referred to as VHB), 3M] because it was transparent, sticky, easily available, and capable of handling large strain (*33*). Although there were limited choices for VHB thickness and VHB was not purposely optimized for DEA applications, the use of VHB provided a balance between ease of preparation and optical/actuation performance. Silicone-based elastomers, which are also transparent, offer more precise control, greater temperature stability, and very low hysteresis, but their use requires additional processing steps.

Transparent, stretchable electrodes were prepared from SWCNTs. A controlled, uniform distribution of SWCNT mats was achieved using a water-based SWCNT dispersion and filtration method. This method produced SWCNT mats on a polytetrafluoroethylene filter that could be directly transferred onto elastomers by pressing them and patterning them with a mask. Applications of DEAs for in-line optical devices required the optimal density of SWCNTs (*28*). A low density was desired to minimize the optical absorption and mechanical stiffening of the actuator. However, a higher density was needed to maintain electrical percolation (particularly for large-area actuation) and to minimize the RC (resistive-capacitive) constant.

To transfer a metasurface from its substrate to the elastomer membrane, we used a sacrificial layer. It was important for the sacrificial layer to be soluble in a solvent orthogonal to both the metasurface and the elastomer such that the solvent only dissolved the sacrificial layer but not the metasurface or the elastomer. We chose germanium dioxide (GeO_2) as the sacrificial layer because it could be readily dissolved in water. Water enables versatility in the use of the process such as in a wide variety of metasurface materials and membrane materials, as well as in other applications.

Device fabrication

A film stack was first prepared for nanofabrication (fig. S2A). Starting with a silicon wafer, we deposited a 0.4-μm layer of elemental germanium (Ge) by electron beam evaporation. The sample was then placed in a furnace (Tystar Tytan) for dry oxidization in the presence of O_2 at atmospheric pressures at 550°C for 3 hours, which converted the layer of Ge into GeO_2, completing the sacrificial layer. We found that the GeO_2 layer made by dry-oxidizing Ge was significantly more soluble in water than were layers deposited by either electron evaporation or thermal evaporation directly using GeO_2 as the source material, possibly due to formation of GeO_x species at high temperatures. GeO_2 also dissolved much faster in water than did Ge in hydrogen peroxide (H_2O_2) and water solution, in which the rate-limiting step was the oxidation of Ge into GeO_2 by H_2O_2. The metasurface itself was composed of nanoposts made of amorphous silicon (a-Si) with a height of 950 nm, so a layer of a-Si with the corresponding thickness was deposited using plasma-enhanced chemical vapor deposition.

In preparation for photolithography, the sample surface was first spin-coated with the adhesion promoter hexamethyldisilazane at 4000 rpm. Next, a 1-μm layer of i-line photoresist (SPR700-1.0, DOW) was spun-coated and soft-baked at 95°C for 60 s. Over the photoresist, a layer of photobleachable contrast enhancement material (CEM365iS, Shin-Etsu MicroSi) was spun-coated at 4000 rpm to improve feature contrast for the following stepper exposure.

The metasurface design (fig. S3) was patterned into the photoresist using stepper photolithography, which allowed us to produce large-area metalenses with high yields. A quartz photomask was patterned using a high-resolution laser lithography system (DWL 2000, Heidelberg Instruments). This photomask was then used as a reticle in a 5× reduction i-line stepper (GCA AS200 AutoStep) to expose the photoresist. After exposure, the CEM365iS layer was removed by spraying deionized water (DIW) and spin drying. The sample was then postexposure-baked at 115°C for 60 s. The photoresist was then soaked in a developer (MF CD-26) for 90 s and rinsed in DIW. Mild O_2 plasma descum was performed to improve pattern fidelity.

The photoresist pattern was used as an etch mask to create the metasurface in the a-Si layer. The sample was etched using an inductively coupled plasma (ICP) reactive ion etch (RIE) system (STS MPX/LPX ICP RIE), in which the etchant gases used were perfluorocyclobutane (C_4F_8) and sulfur hexafluoride (SF_6). The pattern was etched completely through the a-Si layer and as much as 100 nm into the sacrificial layer. Finally, the photoresist was removed by soaking the sample in *N*-methyl-2-pyrrolidone solution (Remover PG, Microchem) for 8 hours, followed by a dry resist strip in a high-temperature (200°C) and high-power (500 W) O_2 plasma asher (Matrix Plasma Asher) for 20 s, leaving a-Si and GeO_2 exposed (fig. S2B).

A membrane of the elastomer (VHB) was uniformly biaxially stretched (four times, linearly) and mounted by its own adhesion on a rigid circular plastic ring to create the DEA. SWCNT electrodes were then applied to either side of the membrane (~30 μm thick).

The simplest electrode configuration (single area) is a disk of SWCNTs concentrically applied to both sides of the membrane in equal areas to produce a single uniform deformation region. More complex electrode configurations were made by patterning multiple electrodes on the same membrane, for instance, by putting multiple addressable patches on one side of the membrane and a common ground electrode on the other side. We fabricated two kinds of electrode patterns: (i) a single area and (ii) a five-segment area. The five-segment device allowed for the creation and control of different strain fields, including radial expansion and contraction strains in the center, uniaxial strain in both x and y directions, and rigid-body displacements in both directions.

A mask for producing the electrode pattern was created by cutting (using a computer numerically controlled cutter) out a stencil of the desired electrode configuration in a polyethylene terephthalate film coated with nonstick silicone. This mask was first applied over the elastomer membrane. A thin, uniform layer of SWCNTs was prepared using the vacuum filtration transfer method, in which a water dispersion of SWCNTs was passed through a Teflon filter, depositing a uniform mat of SWCNTs (*28*). The SWCNT mat was then transferred over the mask and membrane by pressing firmly and peeling off the filter and electrode mask, leaving behind the SWCNTs adhered to the membrane.

To transfer the metasurface to the DEA, we first bonded the metasurface and a scaffold membrane (also VHB) together, after which the scaffold membrane was bonded to the DEA. We originally thought that the adhesion between the metasurface and the membrane would be enhanced by cleaning the surface with oxygen plasma treatment to expose dangling bonds in the form of reactive hydroxyl groups. However, we found that the opposite was true: The same dangling bonds also increased hydrophilicity, which allowed the presence of water or humidity to infiltrate and undercut the bonding between the metasurface and the membrane, rendering weak adhesion. Instead, pure isopropyl alcohol was used to clean the surface of the metasurface, and a chemical

adhesion promoter (AP115, 3M) was used to make the metasurface slightly hydrophobic through surface silanization. AP115 was sprayed onto the metasurface and was quickly wiped off using a lint-free cloth to reduce the contact time of the sacrificial layer with the small amount of water present in AP115. Although we did not know the exact chemical contents of AP115, the active ingredient was probably 3-glycidoxypropyltrimethoxysilane. Next, the membrane was pressed onto the metasurface, using a smooth, spherical press made of soft silicone. A spherical press was important in achieving good contact throughout the entire metasurface area because it is capable of overcoming the nanoimprint proximity effect (*34*), by which there is less adhesion in the center than in the periphery when a flat press is used. The entire sample was then heated in an oven at 50°C for 3 hours to improve adhesion (by allowing the membrane polymer to flow) and then cooled to room temperature.

For release, the entire sample was immersed in water (fig. S2A). Dissolution began around the edges of the devices and moved toward the center as water slowly percolated between the nanoposts. The release time of the entire device depended on the device area and varied between minutes and hours. The scaffold membrane with the supported metasurface was then attached to the DEA by gently pressing it. We refer to the scaffold membrane after combination as the IEL. Two types of layered devices, which we refer to as SL and DL devices, were made: the SL device contained an IEL (not prestretched) that was cut to be as small as the metasurface, whereas the DL device contained an IEL (prestretched four times, linearly) with an area equal to the entire DEA, effectively increasing the stiffness of the combination.

In the final step, electrical contacts with the CNT electrodes were made. The SWCNT electrode patches were connected by conductive silver grease to the leads of a conductive carbon tape, which were then connected to wires.

Measurement methods

A tunable laser (HP 8168F) operating between 1440 and 1590 nm was used as the light source. The optical output of this laser was connected to an optical fiber collimator (Thorlabs F810APC-1550), which produced a collimated beam that was 7 mm in diameter. The collimated beam was used to illuminate the device. The polarization of the beam was allowed to wander because the device was designed to be polarization-independent, and no polarization dependence was observed. A high-voltage source (Trek 610E) was used to tune the device. After passing through the device, the light was measured by a conventional horizontal microscope setup: A microscope objective (10× Mitutoyo M Plan Apo NIR infinity corrected objective) and a tube lens (Plano-Convex Lens, $f = 200$ mm) were used to magnify the beam to fully visualize the focal spot on the camera (digital InGaAs, Raptor OWL640). The entire horizontal microscope setup was mounted on a linear motor (NPM Acculine SLP35), which allowed horizontal scanning of the light field with a positional accuracy of 1 μm. This setup (fig. S6, A and B) was used to characterize focal length and focal spot size. To measure the efficiency, we replaced the microscope objective, tube lens, and camera with an optical power meter (Thorlabs PM100D) (fig. S6C). For comparison, the measured focusing efficiency of the metasurface before transfer (fabricated on a fused silica wafer) was 91%, and the difference in device efficiency was attributed to scattering and absorption by the DEA, as well as to imperfections in the transfer process.

Uniform stretching approximation

A lens that focuses normal incident light has the following hyperboloidal phase profile: $\phi_{ideal} = \pm k\left(\sqrt{r^2 + (s^2 f_0)^2} - s^2 f_0\right)$, where we desire a tunable focal length relationship of the form $f = s^2 f_0$. Achieving ϕ_{ideal} requires a stretch profile that depends on the radial position $s_{radial}(r)$. Then, the phase profile of a lens with focal length f_0 that is stretched by s_{radial} undergoes a coordinate transformation $r \rightarrow r/s_{radial}(r)$, such that the resulting phase profile is as follows: $\phi_{radial} = \pm k\left(\sqrt{(r/s_{radial}(r))^2 + f_0^2} - f_0\right)$. To find the stretch profile that produces the target phase profile ϕ_{ideal}, which has a nominal, uniform stretch value s, we can equate $\phi_{radial} = \phi_{ideal}$ and write s_{ideal} in place of s_{radial} (where s_{ideal} is a specific case of s_{radial} that produces ϕ_{ideal}): $\sqrt{(r/s_{ideal}(r))^2 + f_0^2} - f_0 = \sqrt{r^2 + (s^2 f_0)^2} - s^2 f_0$. Solving for s_{ideal}, we find the following: $s_{ideal}(r) = r/\sqrt{r^2 + 2(s^4 - s^2)f_0^2 + 2(1 - s^2)f_0\sqrt{r^2 + (s^2 f_0)^2}}$. To lowest order, we see that $s_{ideal} \approx s$. Although s_{ideal} is not exactly equal to s, their difference is extremely small. Figure S1 (A and B) shows that there is a slight decrease in local stretch as the radial position is moved outward from the center of the lens, using the lens parameters of our experiment ($f_0 = 50$ mm). A nominal stretch of $s = 1.2$ yields a difference of only $\Delta s = 1 \times 10^{-4}$ at a radial position of 3 mm, corresponding to the size of the lens in our device.

Focal length versus voltage relation

Volume conservation of the elastomer requires that $s_x s_y s_z = 1$, where s is the stretch. For isotropic materials under uniaxial compression, $s_x = s_y = s$, where $s = 1 + \varepsilon_L$ (ε_L is the lateral strain) and $s_z = 1 + \varepsilon_z$ (ε_z is the longitudinal strain, that is, in the thickness direction), giving $s^2 = 1/s_z$. For small strain ($\varepsilon_z \lesssim 0.2$), the strain response ε_z of materials under Maxwell's compression stress, $\sigma_M = -\varepsilon E^2$, can be approximated as that of a linear elastic material with Young's modulus (Y): $\varepsilon_z = -\varepsilon E^2/Y$, where E is the electrical field and ε is the permittivity. As $s_z = 1 + \varepsilon_z$ and $f/f_0 = s^2$, the relation of focal length with voltage V is as described in Eq. 3, where t is the instantaneous thickness of the elastomer, which is a function of the applied voltage but can be approximated as a constant because it changes very little (*33*). By writing $b = \varepsilon/(Yt^2)$, the series expansion for small voltages near $V = 0$ gives $f/f_0 = 1/(1 - bV^2) = 1 + bV^2 + b^2V^4 + O(V^6)$. We see that the focal length relation transitions from a quadratic relation (V^2) to a quartic relation (V^4) as the voltage increases: $V_{transition} > b^{-1/2}$ (and to higher orders if V increases further). For example, by taking nominal values for our dielectric layer made of VHB ($\varepsilon_r = 6$, $Y = 1.8$ MPa, and $t = 30$ μm), $V_{transition}$ becomes 5.52 kV.

Aberrations introduced by stretching

In tunable systems, optical aberrations may be augmented or reduced by tuning. With metalenses, spherical aberration using normal incidence illumination is corrected by design. However, when such a metasurface is deformed, the resulting aberration is not obvious. The wavefront aberration function or WAF (WAF = $\phi_{stretched} - \phi_{ideal}$) quantifies the deviation of the resulting phase profile of the stretched metasurface from the ideal phase profile: $\mathrm{WAF} = \pm k\left(\sqrt{(r/s)^2 + f_0^2} - f_0^2\right) \mp k\left(\sqrt{r^2 + (s^2 f_0)^2} - s^2 f_0\right) = \pm k\frac{(1-s^2)r^4}{8f^3 s^6} + O(r^6)$. This equation shows that as the uniform stretch is increased from $s = 1$, WAF increases from 0 until it reaches a maximum aberration (fig. S1C) at $s \approx 1.22$ (for example, for a lens with ø = 6 mm and $f = 50$ mm, the maximum aberration is <0.05 rad at the edge). Upon further stretching, built-in suppression of spherical aberration comes into effect, in which the WAF decays following a quartic function $(r/s)^4$. This allows for highly tunable lens devices with excellent immunity to aberration.

Statistical methods

Statistical data were presented with the means plotted and with error bars indicating 1 SD.

SUPPLEMENTARY MATERIALS

Supplementary material for this article is available at http://advances.sciencemag.org/cgi/content/full/4/2/eaap9957/DC1

fig. S1. Uniform stretch approximation.
fig. S2. DEA platform.
fig. S3. Metalens design elements.
fig. S4. Optical measurements of a DEA, which consists of a prestretched (four times) acrylic elastomer (VHB Tape 4905, 3M) and SWCNT electrodes.
fig. S5. Device design and operation.
fig. S6. Measurement setup.
fig. S7. Fitting measurement of focal length tuning using electrode V_5.
fig. S8. Measurement of *x,y* shift distortion.
fig. S9. Response time measurement.
table S1. Wavefront shaping with Zernike polynomials.
movie S1. Reliability test.

REFERENCES AND NOTES

1. K. Kasunic, *Optical Systems Engineering* (McGraw-Hill Professional, 2011).
2. H. Itoh, N. Matsumoto, T. Inoue, Spherical aberration correction suitable for a wavefront controller. *Opt. Express* **17**, 14367–14373 (2009).
3. L. Li, D. Bryant, T. van Heugten, P. J. Bos, Physical limitations and fundamental factors affecting performance of liquid crystal tunable lenses with concentric electrode rings. *Appl. Opt.* **52**, 1978–1986 (2013).
4. L. Li, D. Bryant, T. Van Heugten, P. J. Bos, Near-diffraction-limited and low-haze electro-optical tunable liquid crystal lens with floating electrodes. *Opt. Express* **21**, 8371–8381 (2013).
5. S. Shian, R. M. Diebold, D. R. Clarke, Tunable lenses using transparent dielectric elastomer actuators. *Opt. Express* **21**, 8669–8676 (2013).
6. N. Hasan, A. Banerjee, H. Kim, C. H. Mastrangelo, Tunable-focus lens for adaptive eyeglasses. *Opt. Express* **25**, 1221–1233 (2017).
7. L. Maffli, S. Rosset, M. Ghilardi, F. Carpi, H. Shea, Ultrafast all-polymer electrically tunable silicone lenses. *Adv. Funct. Mater.* **25**, 1656–1665 (2015).
8. L. Dong, A. K. Agarwal, D. J. Beebe, H. Jiang, Adaptive liquid microlenses activated by stimuli-responsive hydrogels. *Nature* **442**, 551–554 (2006).
9. C. A. López, A. H. Hirsa, Fast focusing using a pinned-contact oscillating liquid lens. *Nat. Photonics* **2**, 610–613 (2008).
10. H. Ren, S. T. Wu, Variable-focus liquid lens. *Opt. Express* **15**, 5931–5936 (2007).
11. A. Mermillod-Blondin, E. McLeod, C. B. Arnold, High-speed varifocal imaging with a tunable acoustic gradient index of refraction lens. *Opt. Lett.* **33**, 2146–2148 (2008).
12. T. Shibaguchi, H. Funato, Lead-lanthanum zirconate-titanate (PLZT) electrooptic variable focal-length lens with stripe electrodes. *Jpn. J. Appl. Phys.* **31**, 3196–3200 (1992).
13. H. W. Babcock, Adaptive optics revisited. *Science* **249**, 253–257 (1990).
14. R. Ragazzoni, E. Marchetti, G. Valente, Adaptive-optics corrections available for the whole sky. *Nature* **403**, 54–56 (2000).
15. N. Ji, Adaptive optical fluorescence microscopy. *Nat. Methods* **14**, 374–380 (2017).
16. N. Yu, P. Genevet, M. A. Kats, F. Aieta, J.-P. Tetienne, F. Capasso, Z. Gaburro, Light propagation with phase discontinuities: Generalized laws of reflection and refraction. *Science* **334**, 333–337 (2011).
17. N. Yu, F. Capasso, Flat optics with designer metasurfaces. *Nat. Mater.* **13**, 139–150 (2014).
18. P. Genevet, F. Capasso, F. Aieta, M. Khorasaninejad, R. Devlin, Recent advances in planar optics: From plasmonic to dielectric metasurfaces. *Optica* **4**, 139–152 (2017).
19. H. S. Ee, R. Agarwal, Tunable metasurface and flat optical zoom lens on a stretchable substrate. *Nano Lett.* **16**, 2818–2823 (2016).
20. S. C. Malek, H. S. Ee, R. Agarwal, Strain multiplexed metasurface holograms on a stretchable substrate. *Nano Lett.* **17**, 3641–3645 (2017).
21. S. M. Kamali, E. Arbabi, A. Arbabi, Y. Horie, A. Faraon, Highly tunable elastic dielectric metasurface lenses. *Laser Photonics Rev.* **10**, 1002–1008 (2016).
22. A. O'Halloran, F. O'Malley, P. McHugh, A review on dielectric elastomer actuators, technology, applications, and challenges. *J. Appl. Phys.* **104**, 71101 (2008).
23. P. Brochu, Q. Pei, Advances in dielectric elastomers for actuators and artificial muscles. *Macromol. Rapid Commun.* **31**, 10–36 (2010).
24. J. Huang, T. Li, C. F. Choon, J. Zhu, D. R. Clarke, Z. Suo, Giant, voltage-actuated deformation of a dielectric elastomer under dead load. *Appl. Phys. Lett.* **100**, 41911 (2012).
25. S. J. A. Koh, T. Li, J. Zhou, X. Zhao, W. Hong, J. Zhu, Z. Suo, Mechanisms of large actuation strain in dielectric elastomers. *J. Polym. Sci. Part B Polym. Phys.* **49**, 504–515 (2011).
26. S. Timoshenko, J. Goodier, *Theory of Elasticity* (McGraw-Hill, 1970).
27. S. Wischnitzer, *Introduction to Electron Microscopy* (Pergamon Press, 1989).
28. S. Shian, R. M. Diebold, A. McNamara, D. R. Clarke, Highly compliant transparent electrodes. *Appl. Phys. Lett.* **101**, 61101 (2012).
29. A. Arbabi, Y. Horie, A. J. Ball, M. Bagheri, A. Faraon, Subwavelength-thick lenses with high numerical apertures and large efficiency based on high-contrast transmitarrays. *Nat. Commun.* **6**, 7069 (2015).
30. T. Töpper, F. Weiss, B. Osmani, C. Bippes, V. Leung, B. Müller, Siloxane-based thin films for biomimetic low-voltage dielectric actuators. *Sens. Actuators A Phys.* **233**, 32–41 (2015).
31. S. Rosset, H. R. Shea, Small, fast, and tough: Shrinking down integrated elastomer transducers. *Appl. Phys. Rev.* **3**, 31105 (2016).
32. H. C. Ko, M. P. Stoykovich, J. Song, V. Malyarchuk, W. M. Choi, C. J. Yu, J. B. Geddes III, J. Xiao, S. Wang, Y. Huang, J. A. Rogers, A hemispherical electronic eye camera based on compressible silicon optoelectronics. *Nature* **454**, 748–753 (2008).
33. R. Pelrine, R. Kornbluh, Q. Pei, J. Joseph, High-speed electrically actuated elastomers with strain greater than 100%. *Science* **287**, 836–839 (2000).
34. S. Landis, N. Chaix, C. Gourgon, C. Perret, T. Leveder, Stamp design effect on 100 nm feature size for 8 inch NanoImprint lithography. *Nanotechnology* **17**, 2701–2709 (2006).

Acknowledgments: We express our gratitude to R. M. Diebold for helpful discussions about dielectric elastomers; G. Zhong for help in using the Center for Nanoscale Systems (CNS) facilities; and J. Treichler, A. Windsor, G. Bordonaro, K. Musa, and D. Botsch for their help in using the Cornell NanoScale Science and Technology Facility (CNF). **Funding:** This work was financially supported by the Air Force Office of Scientific Research under MURI: FA9550-12-1-0389. A.S. thanks the Charles Stark Draper Laboratory for support through the Draper Laboratory Fellowship. S.Z. thanks the Agency for Science, Technology and Research, Singapore, for support through the National Science Scholarship. The work of S.S. was supported in part by the NSF through grant CMMI-1333835 and by the Materials Research Science and Engineering Center program of the NSF under award number DMR 1420570. F.C. acknowledges a gift from Huawei Inc. under its HIRP FLAGSHIP program. This work was performed in part at the CNS, a member of the National Nanotechnology Infrastructure Network, which was supported by the NSF under NSF award number ECS-0335765. The CNS is part of Harvard University. This work was performed in part at the CNF, a member of the National Nanotechnology Coordinated Infrastructure, which was supported by the NSF (grant ECCS-1542081). **Author contributions:** A.S., S.Z., and S.S. fabricated the materials and devices. A.S. and S.Z., with assistance from S.S., performed the simulations, measurements, and analysis. A.S. and S.Z. wrote the manuscript. F.C. and D.R.C. supervised the project. All authors discussed the results and commented on the manuscript. **Competing interests:** A.S., F.C., D.R.C., S.Z., and S.S. are inventors on a Patent Cooperation Treaty patent application related to this work (number US17/36897, filed 9 June 2017). The authors declare no other competing interests. **Data and materials availability:** All data needed to evaluate the conclusions in the paper are present in the paper and/or the Supplementary Materials. Additional data related to this paper may be requested from the authors.

Submitted 19 September 2017
Accepted 22 January 2018
Published 23 February 2018
10.1126/sciadv.aap9957

Citation: A. She, S. Zhang, S. Shian, D. R. Clarke, F. Capasso, Adaptive metalenses with simultaneous electrical control of focal length, astigmatism, and shift. *Sci. Adv.* **4**, eaap9957 (2018).

Science Advances

Adaptive metalenses with simultaneous electrical control of focal length, astigmatism, and shift

Alan She, Shuyan Zhang, Samuel Shian, David R. Clarke and Federico Capasso

Sci Adv **4** (2), eaap9957.
DOI: 10.1126/sciadv.aap9957